OPEN ACCESS



X-Rays from RS Ophiuchi's 2021 Eruption: Shocks In and Out of Ionization Equilibrium

Nazma Islam^{1,2}, Koji Mukai^{1,3}, and J. L. Sokoloski⁴

Center for Space Science and Technology, University of Maryland, Baltimore County, 1000 Hilltop Circle, Baltimore, MD 21250, USA; nislam@umbc.edu

2 X-ray Astrophysics Laboratory, NASA Goddard Space Flight Center, Greenbelt, MD 20771, USA

² X-ray Astrophysics Laboratory, NASA Goddard Space Flight Center, Greenbelt, MD 20771, USA
 ³ CRESST II and X-ray Astrophysics Laboratory, NASA Goddard Space Flight Center, Greenbelt, MD 20771, USA
 ⁴ Columbia Astrophysics Laboratory, Columbia University, New York, NY 10027, USA
 Received 2023 October 8; revised 2023 November 17; accepted 2023 November 24; published 2024 January 9

Abstract

The recurrent nova RS Ophiuchi (RS Oph) underwent its most recent eruption on 2021 August 8 and became the first nova to produce both detectable GeV and TeV emission. We used extensive X-ray monitoring with the Neutron Star Interior Composition Explorer Mission (NICER) to model the X-ray spectrum and probe the shock conditions throughout the 2021 eruption. The rapidly evolving NICER spectra consisted of both line and continuum emission that could not be accounted for using a single-temperature collisional equilibrium plasma model with an absorber that fully covered the source. We successfully modeled the NICER spectrum as a nonequilibrium ionization collisional plasma with partial covering absorption. The temperature of the nonequilibrium plasma shows a peak on day 5 with a kT of approximately 24 keV. The increase in temperature during the first five days could have been due to increasing contribution to the X-ray emission from material behind fast polar shocks or a decrease is the amount of energy being drained from the shocks into particle acceleration during that period. The absorption showed a change from fully covering the source to having a covering fraction of roughly 0.4, suggesting a geometrical evolution of the shock region within the complex global distribution of the circumstellar material. These findings show evidence of the ejecta interacting with some dense equatorial shell initially, and with less dense material in the bipolar regions at later times during the eruption.

Unified Astronomy Thesaurus concepts: Recurrent novae (1366); Plasma astrophysics (1261); Astronomy data analysis (1858); High energy astrophysics (739)

1. Introduction

Novae are transient systems containing a white dwarf (WD) accreting matter from a nondegenerate stellar companion. These systems go into eruption when the accreted matter undergoes thermonuclear runaway (TNR) on the surface of the WD. The TNR releases a large amount of energy, which causes the ejection of the accreted matter. If the donor star is a red giant (RG) that produces a wind or focused outflow, the ejecta from the nova can interact with this circum-binary matter (Warner 1995; Bode & Evans 2008; Starrfield et al. 2016).

The recurrent nova RS Ophuichi (RS Oph) consists of a massive WD and an RG donor star in a binary orbit with a period of 453.6 ± 0.4 days (Brandi et al. 2009). The distance estimate to RS Oph in Gaia Data Release 3 is 2.44 kpc (Bailer-Jones et al. 2021); however there is some uncertainty on the Gaia estimate because of the surrounding nebula and the wobble of the long binary period. It has previously undergone nova eruption approximately every 15 yr, with recorded eruptions in 1898, 1933, 1958, 1967, 1985, and 2006 and a possible additional eruption in 1907. RS Oph began its recent eruption on 2021 August 8 as per the discovery in the optical reported in AAVSO Alert Notice 752.5 Subsequently, the eruption was detected across the electromagnetic spectrum: in the radio with the Very Large Array (VLA) Low-band Ionospheric and Transient Experiment (VLITE; Peters et al.

Original content from this work may be used under the terms of the Creative Commons Attribution 4.0 licence. Any further distribution of this work must maintain attribution to the author(s) and the title of the work, journal citation and DOI.

2021), the Jansky VLA (Sokolovsky et al. 2021), the Arcminute Microkelvin Imager Large Array (AMI-LA), e-MERLIN, and MeerKAT (Williams et al. 2021); in the infrared with the NASA Infrared Telescope Facility (Woodward et al. 2021a, 2021b); in the optical with the Southern African Large Telescope (SALT; Mikolajewska et al. 2021), the Varese telescope (Munari & Valisa 2021), among many others; and in X-rays with the Monitor of All Sky X-ray Image (MAXI; Shidatsu et al. 2021), Neil Gehrels Swift Observatory (Swift; Page et al. 2021, 2022), INTErnational Gamma-Ray Astrophysics Laboratory (INTEGRAL; Ferrigno et al. 2021), Neutron Star Interior Composition Explorer (NICER; Enoto et al. 2021), Nuclear Spectroscopic Telescope Array (NuS-TAR; Luna et al. 2021), AstroSat (Rout et al. 2021), Chandra, and XMM-Newton (Orio et al. 2021). It became the first nova to have detectable TeV/GeV gamma rays, with TeV emission detected by the High Energy Stereoscopic System (HESS; Wagner 2021; H.E.S.S. Collaboration et al. 2022) and the Major Atmospheric Gamma Imaging Cherenkov Telescopes (MAGIC; Acciari et al. 2022) and GeV emission detected with Fermi-LAT (Cheung et al. 2021, 2022).

Unlike in majority of novae hosted in cataclysmic variables, the donor star in RS Oph is an RG, and the high-velocity ejecta from the TNR runs into its dense stellar wind, giving rise to X-ray emission from hot, shocked gas. In this and prior eruptions, the initial X-ray emission was dominated by hard emission in the 1–10 keV energy range thought to originate from such shocks, analogous to hard X-ray emitting shocks seen in supernova remnants (Vink 2012). RS Oph thus provides an excellent laboratory to study the interaction of the ejecta with the stellar winds from the donor star. After the nova ejecta expand and become optically thin to soft X-rays,

https://www.aavso.org/aavso-alert-notice-752

the X-ray emission is generally dominated by a blackbody-like supersoft component originating in the photosphere of the nuclear shell-burning WD with a kT corresponding to an effective temperature of 20–100 eV.

From numerical simulations of RS Oph in quiescence and during eruption, we expect the quiescent mass transfer to produce a ring-like equatorial density enhancement, with which the ejecta interact and produce a bipolar outflow (Booth et al. 2016). The Rossi X-ray Timing Explorer (RXTE) Proportional Counter Array (PCA) observations of the 2006 eruption of RS Oph indeed suggested that the hard X-ray emission from that event faded at a rate that was consistent with an X-rayemitting volume increasing roughly as the square of the blast wave radius, as expected for a shock moving into an equatorial ring (O'Brien et al. 2006; Sokoloski et al. 2006; Orlando et al. 2009). Radio imaging weeks to months after the beginning of the 2006 eruption revealed an asymmetric shock wave, with a bipolar jet-like outflow and possible equatorial enhancement in the RG wind (O'Brien et al. 2006; Rupen et al. 2008; Sokoloski et al. 2008). Optical imaging of the RS Oph nebular remnant using the Hubble Space Telescope and ground-based observations showed that the remnant consisted of two distinct components—a high-density, low-velocity RG wind in the equatorial regions of the binary, and an extended, high-velocity structure at the poles (Ribeiro et al. 2009). Finally, extended X-ray emission observed by Chandra after the 2006 eruption was consistent with the bipolar outflows seen in the radio and optical imaging (Montez et al. 2022). So, radio, optical, and X-ray observations after the 2006 eruption support the picture of RS Oph as having a density enhancement near the equatorial plane that plays a role in shaping the nova shocks and ejecta.

During the 2021 eruption of RS Oph, NICER continuously monitored from day 2 through day 90 after the beginning of the eruption, with exposure times ≥ 1 ks. An analysis of the NICER data using a collisional equilibrium plasma model have already been published by Orio et al. (2023). This paper presents an independent analysis in which we explore the need for emission from a nonequilibrium ionization (NEI) collisional plasma to explain the observed X-ray emission.

2. NICER and MAXI Observations and Data Reduction

NICER is an X-ray observatory that has been operating on the International Space Station (ISS) since 2017 (Gendreau et al. 2016). The main instrument, the X-ray Timing Instrument (XTI), consists of 56 identical and coaligned cameras, each containing an X-ray Concentrator (XRC; Okajima et al. 2016) and an Si drift detector positioned in the concentrator's focal plane. During the 2021 eruption of RS Oph, NICER monitored the progress of the eruption with almost daily exposures of between approximately 1 and 10 ks from 2021 August 10 to November 7, until RS Oph entered the solar observing constraint. We analyzed the NICER data using nicerversion 2022 December 16 _ V010a, released with HEAsoft v6.31.1 and calibration files xti20221001. The standard pipeline processing was used to carry out screening and filtering of data and apply the latest calibration files using nicer12. Using NICERDAS task nicer13-spect, we extracted the source, the background spectrum, and the appropriate response matrices and ancillary files. The source spectrum was automatically rebinned with nicer13-spect using ftgrouppha with the optimal binning method (Kaastra & Bleeker 2016). We carried out the spectral analysis by fitting

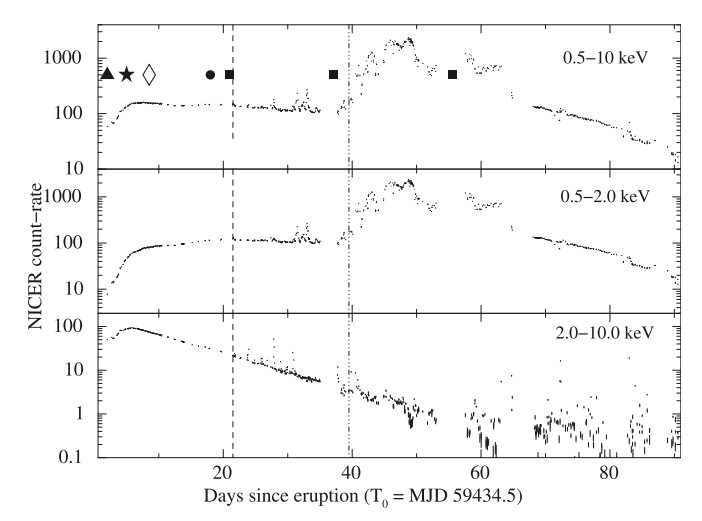


Figure 1. NICER lightcurves of RS Oph in units of counts s⁻¹, plotted from the beginning of the eruption ($T_0 = \text{MJD} 59434.5$), with 1000 s bins. The top panel shows the lightcurve in the 0.5–10 keV band, the middle panel in the 0.5–2.0 keV band, and the bottom panel in the 2–10 keV energy band. The dashed line at day 21 marks the beginning of the supersoft phase as reported by Page (2021). The dotted–dashed line at day 40 shows the beginning of the highly variable supersoft phase, during which the 0.5–10 keV and 0.5–2.0 keV lightcurves show rapid brightness variations by a factor of 10 or more. The triangle denotes the time of the peak of the Fermi-LAT lightcurve on day 2, the star shows the time of the peak of the HESS lightcurve on day 5, the rhombus indicates the time of the NuSTAR observation carried out on day 8, the circle indicates the time of the Chandra HETG observation on day 18 (Orio et al. 2022), and the squares show the times of the XMM observations on days 21, 37, and 55 (Orio et al. 2022; Ness et al. 2023).

the source spectrum and modeling the background spectrum using the SCORPEON background model. The NICER spectrum was analyzed in the energy range 0.5–10.0 keV and a systematic error of 3% was added in quadrature during the spectral fits to account for the possible uncertainties due to dust scattering effects around RS Oph (Smith et al. 2016). Using the NICERDAS task nicerl3-lc with the Space Weather model for the background, we extracted background-subtracted lightcurves in different energy bands (0.5–10, 0.5–2, and 2–10 keV). All times are relative to the start of the optical eruption at $T_0 = \text{MJD}$ 59434.5 (Munari & Valisa 2021).

The NICER lightcurves reveal variations in the X-ray brightness throughout the eruption. Figure 1 show lightcurves constructed from the NICER observations in the 0.5-10 keV (broad), 0.5-2 keV (soft), and 2-10 keV (hard) energy bands. The lightcurves in the broad, soft, and hard energy bands all show rapid increases in count rate through day 6 and then remain at a similar count-rate level through day 21 in the broad and soft bands. The dashed line at MJD 59456 (day 21) in Figure 1 marks the beginning of the supersoft phase as reported by Page (2021). The count rate in the hard band monotonically decreased after reaching its peak around day 6. The count rate in the soft band dominated the total X-ray emission from day 20 onwards. The dotted-dashed line at MJD 59474 (day 40) in Figure 1 indicates the beginning of the highly variable supersoft phase, during which the broad and soft lightcurves show rapid brightness variations by a factor of 10 or more, especially in the soft band. The contribution to the overall

⁶ https://heasarc.gsfc.nasa.gov/docs/nicer/analysis_threads/scorpeon-xspec/

https://heasarc.gsfc.nasa.gov/docs/nicer/analysis_threads/nicerl3-lc/

Table 1Summary of NICER Observations

ObsID	Start Time	End Time	Total Exp. (ks)	Avg. Count Rate
4202300101	2021-08-10T11:55:17	2021-08-10T12:14:20	1.02	59.3
4202300102	2021-08-11T04:56:00	2021-08-11T23:41:35	2.62	70.5
4202300103	2021-08-12T01:08:00	2021-08-12T22:55:55	2.63	98.9
4202300104	2021-08-13T03:27:10	2021-08-13T23:42:22	3.88	134.6
4202300105	2021-08-14T01:09:01	2021-08-14T22:59:20	3.97	154.8
4202300106	2021-08-15T03:29:31	2021-08-15T23:46:19	6.16	156.5
4202300107	2021-08-16T01:11:22	2021-08-16T22:58:13	3.85	157.4
4202300108	2021-08-17T01:59:02	2021-08-17T23:47:19	3.84	154.4
4202300109	2021-08-18T01:13:09	2021-08-18T23:00:46	2.98	151.7
4202300110	2021-08-19T20:38:03	2021-08-19T22:26:11	1.04	145.2
4202300111	2021-08-20T21:26:19	2021-08-20T23:15:38	1.27	140.6
4202300112	2021-08-21T00:31:00	2021-08-21T00:48:38	0.92	140.7
4202300113	2021-08-21T23:47:07	2021-08-22T09:39:08	9.61	141.3
4202300114	2021-08-23T16:05:56	2021-08-23T17:41:20	0.41	141.1
4202300115	2021-08-24T15:21:31	2021-08-24T15:54:06	1.36	144.0
4202300116	2021-08-25T16:14:40	2021-08-25T16:49:00	1.41	147.4
4202300117	2021-08-26T07:41:00	2021-08-26T08:19:20	2.18	146.2
4202300118	2021-08-28T01:46:00	2021-08-28T05:17:40	1.53	145.2
4202300119	2021-08-30T00:05:00	2021-08-30T10:01:20	9.51	142.6
4202300120	2021-08-31T02:25:17	2021-08-31T05:46:34	2.45	135.2
4202300121	2021-09-01T04:47:35	2021-09-01T11:13:20	3.89	143.6
4202300122	2021-09-02T00:56:40	2021-09-02T23:00:49	4.47	132.6
4202300123	2021-09-03T00:11:33	2021-09-03T23:47:00	6.69	140.6
4202300124	2021-09-04T07:12:00	2021-09-04T21:31:40	2.62	149.1
4202300125	2021-09-05T01:56:40	2021-09-05T23:54:20	7.08	160.3
4202300126	2021-09-06T01:02:33	2021-09-06T23:27:00	8.84	124.2
4202300127	2021-09-07T02:17:00	2021-09-07T23:52:40	7.73	126.4
4202300128	2021-09-08T02:36:03	2021-09-08T23:19:20	8.33	196.7
4202300129	2021-09-09T02:17:20	2021-09-09T23:53:00	8.59	227.4
4202300130	2021-09-10T02:41:20	2021-09-10T23:26:40	9.75	303.3
4202300131	2021-09-11T02:16:40	2021-09-11T22:35:20	6.73	148.7
4202300132	2021-09-12T03:03:27	2021-09-12T12:28:20	2.16	157.7
4202300133	2021-09-15T03:31:21	2021-09-15T20:46:40	2.03	193.7
4202300134	2021-09-16T01:13:34	2021-09-16T23:12:20	4.41	304.4
4202300135	2021-09-17T03:35:00	2021-09-17T14:44:00	3.04	307.9

X-ray emission from the hard band was negligible after the source entered the highly variable supersoft phase and hence we carry out analysis until day 40. Table 1 show the details of the NICER observations used in this paper.

MAXI is an all-sky X-ray monitor that has been operating on the ISS since 2009 (Matsuoka et al. 2009). The main instrument on board is the Gas Slit Camera (GSC), which consists of six units of large-area, position-sensitive Xenon proportional counters in the energy range 2-30 keV, and has an instantaneous field of view of $1.5 \times 160^{\circ}$. It covers 85% of the entire sky approximately every 92 minutes i.e during one ISS orbit. The in-orbit performance of GSC is summarized in Sugizaki et al. (2011). We extracted the lightcurve in the 10-20 keV energy band starting around the beginning of the 2021 eruption using MAXI on-demand data⁸ with a bin time of 5400 s. Figure 2 shows this MAXI/GSC lightcurve. The source was outside the MAXI/GSC field of view when the optical eruption was reported on MJD 59434.5. There was an increase in the X-ray count rate observed with MAXI GSC above 10 keV in the first seven days of the eruption, with the peak of the X-ray intensity occurring at around days 4–7.

3. Results: Fits to the NICER Spectra

3.1. Shortcomings of Single-temperature APEC Models

The early hard X-ray emission seen during the previous 2006 eruption of RS Oph was attributed to a shock interaction between the nova ejecta (violently ejected from the WD surface at several thousand kilometers per second) and the dense wind of the RG (Bode et al. 2006; Sokoloski et al. 2006). To fit the low-spectral-resolution RXTE data, Sokoloski et al. (2006) used a model consisting of Bremsstrahlung continuum emission plus a Gaussian for the blended Fe emission lines. Bode et al. (2006) used a mekal plasma code to fit the Swift XRT data, with its typical CCD resolution but comparably modest statistical quality. With the excellent spectral sensitivity of NICER compared to RXTE PCA and Swift XRT, the NICER spectrum demands a complex spectral model.

Figure 3 shows an example fit to the NICER spectrum taken around day 11 with a single-temperature, collisionally ionized plasma model with variable abundances and velocity-broadened and thermally broadened emission lines (bvapec); the emission component was convolved with the fully covering photoelectric absorption model Tbabs. The residuals from the single-temperature bvapec model fit show considerable structures around the observed K-shell lines from medium-Z

⁸ http://maxi.riken.jp/mxondem/index.html

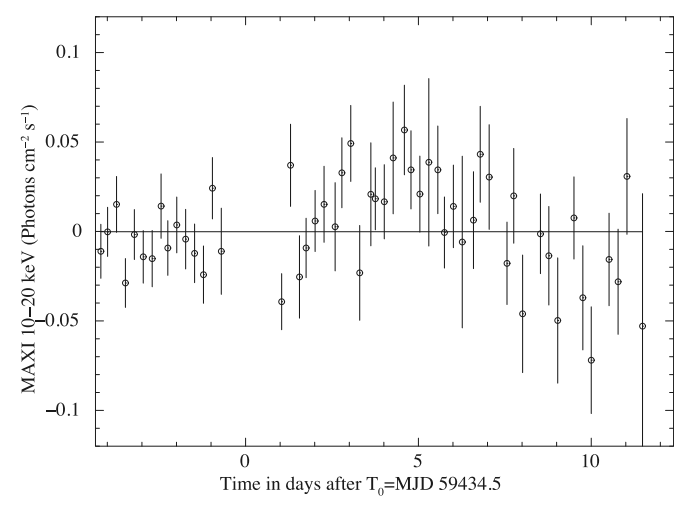


Figure 2. MAXI GSC lightcurve of RS Oph in the $10-20 \, \text{keV}$ energy band, extracted with 5400 s bins. Consistent with the shape of the NICER lightcurves (which are at lower energies), there is a slight enhancement in the X-ray intensity around days 4–7.

elements such as Ne, Mg, and Si. The continuum shape of the spectrum suggests an electron temperature of 3.9 keV, in which case these elements, if in ionization equilibrium, would be expected to be fully ionized and therefore produce only weak emission lines. However, the data show strong K-shell lines from medium-Z elements such as Ne, Mg, and Si, suggesting that these elements were not fully ionized. The other problem with the single-temperature, collisional equilibrium plasma model with a single absorber is the presence of strong lowenergy residuals below roughly 1 keV, as seen in middle panel of Figure 3. The addition of one lower-temperature component can help with the medium-Z lines if the temperature is near the peak emissivity of these lines ($kT \approx 1-2 \text{ keV}$) or the lowenergy residuals if the temperature is very low (kT < 0.5 keV), but a single additional broadband emission component cannot solve both problems. Page et al. (2022) and Orio et al. (2022) chose to add a lower-temperature collisional equilibrium plasma model to account for the medium-Z lines in their analysis of the Swift/XRT, Chandra HETG, and XMM/RGS spectra of RS Oph during its 2021 eruption. However, twotemperature APEC models with a fully covering photoelectric absorber or a partial covering absorber fail to fit the NICER spectrum during the early days of the eruption (up to day 5), as mentioned in Orio et al. (2023).

3.2. Nonequilibrium Collisional Plasma Models

The fits to the NICER spectra using single-temperature or two-temperature APEC models suffer inadequacies in modeling the emission from the K shells of medium-Z elements like Ne, Mg, and Si, as well as the continuum emission below $\sim 1 \text{ keV}$. As previously noted by Nelson et al. (2012) in the context of V407 Cyg, another nova eruption in a symbiotic binary, the existence of a second, low-temperature plasma is not the only possible explanation for the presence of medium-Z lines in an X-ray spectrum.

We took an alternative approach of using NEI collisional plasma models. This approach is often found to be necessary in modeling the X-ray spectra of supernova remnants (e.g., Bamba et al. 2005; Badenes et al. 2006). In astrophysical shocks, the ions that encounter a shock are initially less ionized

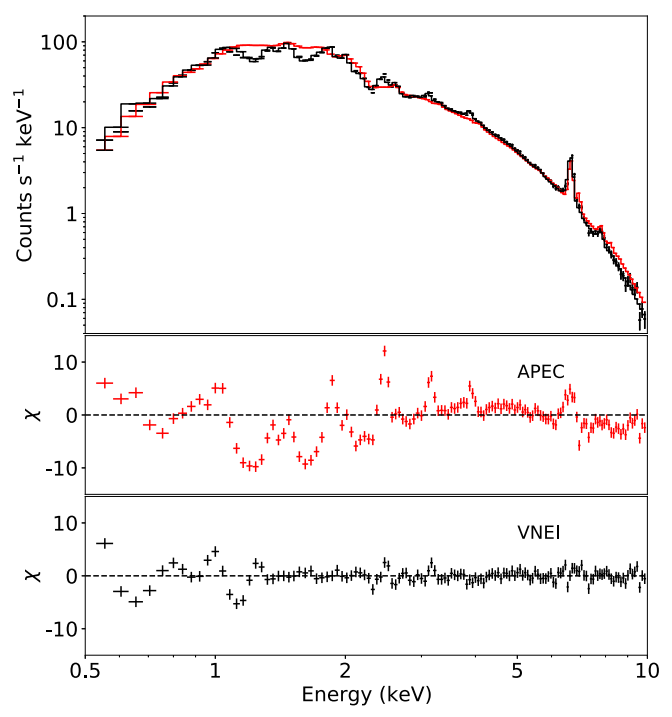


Figure 3. NICER spectrum of RS Oph taken around day 11. The top panel shows the NICER spectrum fitted with a single-temperature, velocity-broadened and thermally broadened collisional equilibrium plasma emission bvapec model convolved with the fully covering photoelectric absorption model Tbabs (red lines) and a model consisting of a grid of nonequilibrium vnei components described in Section 3.2 (black line). The middle panel show the residuals for the spectral fit for the single-temperature bvapec model with fully covering photoelectric absorption. The bottom panel show the residuals for the spectral fit using the NEI grid model. The y-axes on both residual plots use the same range.

and do not reach the equilibrium ionization level until the density-weighted timescale of the plasma, nt, is of order $10^{12} \,\mathrm{s\,cm^{-3}}$, where n is the electron density and t is the equilibrium timescale (Smith & Hughes 2010). The clock time required to reach ionization equilibrium is inversely proportional to the plasma density, so it is the product nt that describes the degree of departure from the ionization equilibrium. If nt is greater than $10^{12} \,\mathrm{s\,cm^{-3}}$, then the plasma can be considered to be in ionization equilibrium. Values much lower than $10^{12} \,\mathrm{s\,cm^{-3}}$ indicate that NEI effects are important. If the X-ray emission originates from low-density and/or freshly shocked matter, it is possible for a plasma with $kT \ge 10 \,\mathrm{keV}$ to nevertheless emit the K-shell emission lines from Ne, Mg, and Si lines.

We considered several options for the inclusion of NEI effects. Orio et al. (2023) modeled the NICER spectra taken during the initial days of the eruption, through to day 5, with a nonequilibrium collisional plasma model, vpshock. While Orio et al. (2023) ruled out the vpshock model after day 5, we believe that their analysis does not rule out NEI effects in general. vpshock is a plane-parallel shock model that incorporates NEI physics and is appropriate for supernova remnants in the Sedov–Taylor phase (Borkowski et al. 2001). In this model, the supernova remnant is assumed to be a point-like blast wave expanding into a uniform ambient medium, resulting in a linear distribution of ionization timescale versus emission measure (EM). Given the complicated distribution of the RG wind around the WD in the RS Oph system, it is not clear that this linear distribution would be a good

approximation. We therefore constructed a model that mimics a similar single-temperature, multiple-ionization timescale NEI plasma using a grid of vnei components in xspec (vnei models are appropriate for single-temperature, single-ionization timescale NEI plasma). We take the temperature to be identical among all vnei components, but leave the normalizations free to vary independently, thus allowing the grid to approximate an arbitrary distribution of EMs as a function of ionization timescale. After several trials, we decided to implement a grid of four vnei components, with the density-weighted ionization timescales of 10^9 , 10^{10} , 10^{11} , and 10^{12} in units of s cm⁻³ and the temperatures of all the vnei components tied to a single temperature. Furthermore, we opted to use a partial covering absorber instead of a second, lower-temperature plasma to account for the low-energy residuals. We considered the NICER spectrum to be attenuated by two absorption components: (1) a variable absorption component from the RG wind and unshocked ejecta ($N_{\rm Hw}$) that only partially cover the source, modeled by Tbpcf; and (2) a component due to photoelectric absorption along the line of sight, modeled by Thabs $(N_{\rm H})$. This component models absorption due to the interstellar medium (ISM) as well as a part of the intrinsic absorption that fully covers the emission region. After day 20, the fits to the NICER spectrum in 0.5-10 keV energy range were unable to constrain both $N_{\rm H}$ and $N_{\rm Hw}$. Hence, we fixed $N_{\rm H}$ to the ISM value of 2.4×10^{21} cm⁻² (Hjellming et al. 1986), which is the minimum $N_{\rm H}$ expected along the line of sight to RS Oph. We used the Gaussian smoothing model gsmooth to account for the velocity broadening of the emission lines. The full spectral model used was:

Tbpcf * Tbabs * gsmooth(vnei + vnei + vnei + vnei).

We let the abundances of N, Si, Ne, Mg, and Fe remain as free parameters, except for fits where these abundances could not be constrained. While the Fe features are strong and allow its abundance to be estimated, the Ni features are weaker, and it is more difficult to constrain its abundance. However, if the Fe abundance is allowed to vary while the Ni abundance is fixed at the solar value, the latter may interfere with accurately determining the former (particularly if Fe is significantly underabundant compared to the solar value). The observed [Ni/Fe] ratio in Galactic stars are found to be similar to solar abundances and these elements likely originate from the same astrophysical processes (Eitner et al. 2023). We link the Fe and Ni abundances in our spectral fits so that the [Ni/Fe] ratio is constant at the solar ratio and the Fe abundance is estimated from the spectral fits. After day 18, both the Ni and Fe abundances are fixed to solar values. The number of free parameters for the above vnei grid model is about 12 (assuming only two elemental abundances are kept free in any spectral fit), which is not significantly different from the 11 and 15 free parameters in the two-temperature byapec model fits to the NICER and Chandra HETG data, respectively (Orio et al. 2021, 2022), and less than the 17 free parameters in the three-temperature byapec model fits to the XMM RGS spectra (Orio et al. 2022).

The bottom panel of Figure 4 shows the residuals to the fit for an example NICER spectrum around day 11, with the above NEI grid with a partial covering absorber model. Compared to the fits using a single temperature, fully covering APEC model (middle panel of Figure 3), there is an improvement in the residuals at low energies and around the emission lines of Ne,

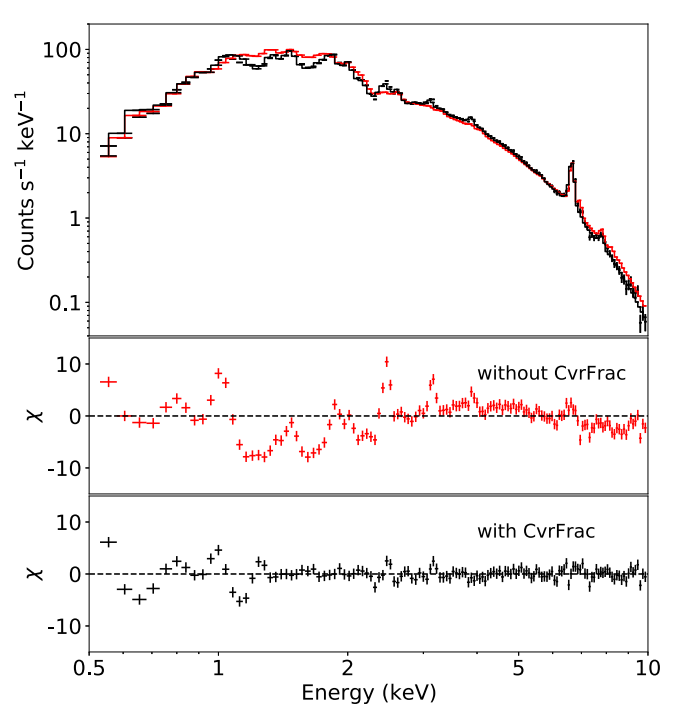


Figure 4. NICER spectrum of RS Oph taken around day 11. The top panel shows the NICER spectrum fitted with a model consisting of a grid of nonequilibrium vnei components described in Section 3.2, without partial covering absorption (red lines) and with partial covering Tbpcf absorption (black lines). The middle panel show the residuals of the spectral fit using the NEI grid model without a partial covering absorber. The bottom panel shows the residuals of the spectral fit using the NEI grid model with a partial covering absorber. The y-axes on both residuals plots use the same range.

Si, Mg, and Fe. The middle panel of Figure 4 show the residuals of the fit to a NICER spectrum with the above NEI grid model without a partial covering absorption component. We see strong residuals at energies below about 2 keV, which reduce with the use of a partial covering absorption model.

Finally, to retain our focus on X-rays from the shocked plasma in RS Oph rather than emission from the WD surface, we only modeled the NICER spectrum above 1.5 keV once the flux at the lower energies started to increase due to the emerging supersoft emission around day 32. For the NICER spectra before day 32, we used the above NEI grid model in the full energy range of 0.5-10.0 keV. After day 32, the contribution of the flux in the soft X-ray band, 0.5-2.0 keV, increased due to the emerging soft emission (and soft X-ray flares as seen in Figure 1). The NEI grid model with the partial covering absorber became insufficient in modeling the NICER spectrum; below 1.5 keV, there are strong residuals that would require additional complex spectral modeling with WD atmosphere models as demonstrated in Page et al. (2022), which is beyond the scope of this work. Hence, we fit the NICER spectrum in the energy range 1.5–10 keV after day 32. The spectral model we used was Tbabs *gsmooth(vnei+ vnei + vnei + vnei).

The NICER spectra above $1.5 \, \text{keV}$ are not sensitive to variations in the absorption, therefore we fixed $N_{\rm H}$ to the ISM value of $2.4 \times 10^{21} \, \text{cm}^{-2}$. We also fixed the abundance of N at solar since the N emission lines are below $1.5 \, \text{keV}$ and cannot be constrained by the NEI grid model for fits above $1.5 \, \text{keV}$. After day 40, the source entered a highly variable supersoft phase (Figure 1), during which the contribution of the hard X-rays to the spectrum above $1.5 \, \text{keV}$ was not significant

enough to allow for NEI grid model fitting. Therefore we report results only up to the beginning of the highly variable supersoft phase. Table 2 reports the results of the spectral fits to the NICER spectra using the above spectral model, along with error bars reported as 90% confidence limits. Orio et al. (2023) reported for their data from MJD 59442 unabsorbed X-ray flux in the 0.2-10 keV energy band of 2.2×10^{-9} erg s⁻¹ cm⁻² using the 2T byapec model and 7.6×10^{-9} erg s⁻¹ cm⁻² with the NEI vpshock model. For a distance of 2.4 kpc, this corresponds to an unabsorbed X-ray luminosity of 1.5×10^{36} and $5.3 \times 10^{36} \text{ erg s}^{-1}$ for the $2 \tilde{T}$ byapec and vpshock models, respectively. For the same date, we report an unabsorbed X-ray flux at $0.2-10 \,\mathrm{keV}$ (extrapolated from the $0.5-10 \,\mathrm{keV}$ spectral fit) of $3.6 \times 10^{-9} \,\mathrm{erg \ s^{-1} \ cm^{-2}}$. For a distance of 2.4 kpc, the unabsorbed X-ray luminosity is 2.5×10^{36} erg s⁻¹, which is not as high as the previously reported unabsorbed X-ray luminosity using the vpshock model.

Figure 5 further demonstrates the need for NEI models. It shows a portion of a NICER spectrum from the early days of the eruption around day 4, near the He- and H-like Fe lines at around 6.7 and 6.9 keV, respectively. The temperature determined from the continuum shape of the spectrum of the plasma was 17 keV, so if the plasma was in ionization equilibrium, we would expect the Fe atoms to be fully ionized. We fit the NICER spectrum around the H- and He- like Fe lines in two ways: using the NEI grid model described above, and using a two-temperature APEC model. As seen from Figure 5, both models describe qualitatively the peak around 6.7 keV and predict a higher flux than observed around the 6.97 keV line. However, the NEI grid model is found to fit the rising part of the 6.7 keV line (6.1–6.4 keV) better than the two-temperature APEC model. The reason we were unable to fit the He-like and H-like Fe lines is likely our chosen spacing of ionization timescales $(10^9, 10^{10}, 10^{11}, and 10^{12})$ in units of s cm⁻³). The Fe K complex in an NEI model with kT = 17 keV and $nt = 10^{12} \,\mathrm{s \, cm^{-3}}$ is dominated by the H-like Fe line at 6.97 keV with a much weaker He-like line at 6.7 keV, whereas a kT = 17 keV, $nt = 10^{11} \text{ s cm}^{-3}$ model is dominated by Helike Fe lines with very few H-like Fe lines. The lower nt models contribute the line flux at 6.4 keV. The weakness of the 6.97 keV line in the data shows that there is little near-equilibrium ($nt = 10^{12} \text{ s cm}^{-3}$), kT = 17 keV plasma on day 4, but some plasma above the next highest nt grid point (i.e., $nt > 10^{11} \text{ s cm}^{-3}$) may well be present. However, this constraint is derived only from the three Fe line fluxes, which is insufficient for us to be able to derive a quantitative model of the true EM distribution, since we might need to adjust the spacing of the nt grid.

3.3. Evolution of Spectral Parameters

Figure 6 shows the evolution of the spectral parameters estimated by fitting the above spectral model to the 1 day averaged NICER spectrum. Panel (a) shows the evolution of the nonequilibrium plasma temperature kT (in units of keV). The temperature initially rose, through day 5, when it reached a peak temperature of 24 keV. A similar enhancement in the X-ray intensities around days 4–7 is marginally apparent in the MAXI GSC lightcurve in the 10–20 keV energy band (Figure 2), suggesting that the plasma temperature peak on day 5 was real and not an artifact of spectral modeling. In contrast, the dip in measured kT on days 30–32 is most likely

an artifact of the change in energy band of spectral fitting from 0.5–10 keV to 1.5–10 keV, as discussed in Section 3.2. The temperature evolution after day 5 is reasonably well described by a power law with an index of -0.9 ± 0.1 . This index is not too different to the -0.7 expected for the temperature evolution of plasma heated by a decelerating blast wave moving into a spherically symmetric stellar wind, even though the circumstellar distribution around RS Oph is known to be at least somewhat asymmetrical (Sokoloski et al. 2006).

The EM peaked at around day 6 (a day after the peak in kT) and then monotonically decreased as the eruption progressed. The EM can be approximated as the sum of the normalizations of the four vnei components used in the spectral fitting. Panel (b) of Figure 6 shows the evolution of the EM. After day 6, the decrease in the EM is reasonably well described by a power law with an index of -1.2 ± 0.1 . Panel (c) of Figure 6 shows the evolution of the individual normalizations of the four vnei components: N1 is the normalization of the vnei component with a density-weighted equilibrium timescale of $10^9 \, \mathrm{s\,cm^{-3}}$, N2 is the one with $10^{10} \, \mathrm{s\,cm^{-3}}$, N3 is the one with $10^{11} \, \mathrm{s\,cm^{-3}}$, and N4 is the one with $10^{12} \, \mathrm{s\,cm^{-3}}$. From the earliest days of the eruption through day 17, the values of N3 and N4 were larger than N1 and N2 and then showed a monotonic decline as the eruption progressed. The values of N1 and N2 remained fairly constant throughout the eruption. After day 18, the values of N1 and N2 started to dominate over the values of N3 and N4.

Panels (d) and (e) of Figure 6 show the time evolution of the column density of the intrinsic, variable absorption from the RG wind and the unshocked ejecta ($N_{\rm Hw}$), and the absorption component along the line of sight ($N_{\rm H}$); as well as the degree to which that absorber covered the source of X-ray emission (CvrFrac), respectively. During the first five days of the eruption, $N_{\rm Hw}$ dropped by about a factor of two. It then jumped up by roughly a factor of four around day 6 and then monotonically decreased through day 32, after which we fixed it to the ISM value. The covering fraction (CvrFrac), declined between the start of the eruption and around day 16, when it reached a minimum value of 0.4. After day 18, the spectra were consistent with containing only a fully covering absorber.

We kept the abundances of the NEI grid model fixed to the solar abundance, except for N, Ne, Mg, Si, Fe, and Ni. The abundances of Fe and Ni were tied to each other and spanned a range of 0.9–1.5 Z_{\odot} . Table 2 reports the abundances obtained with the NEI grid model. The abundances of Ne were $0.9–1.0\,Z_{\odot}$, those of Mg were $0.6–2.1\,Z_{\odot}$, and those of Si were $0.7-1.7 Z_{\odot}$. We allowed the abundance of N to vary after the source entered the supersoft state on approximately day 20, and by around day 32 it had reached a value of higher than $50 Z_{\odot}$. After day 32, the spectral fits were carried out at 1.5–10 keV and hence we could not constrain the abundance of N with the spectral fits and it was fixed at 1.0. The fact that our fits do not require large deviation from solar abundances, except for N, is reassuring. The large overabundance of N implies the presence of CNO-processed material, most likely created during the TNR (Sokolovsky et al. 2020).

4. Discussion

4.1. Evolution of Postshock X-Ray Emission in the Context of a Two-zone Model

The evolution of the normalizations for the four vnei components in the NEI grid model suggests that the

Islam, Mukai, & Sokoloski

 Table 2

 Best-fit Spectral Parameters for the NICER Spectra Using the Model Defined in Section 3.2

Days	kT	$N_{ m HW}$	CvrF	$N_{ m H}$	N1	N2	N3	N4	Fe	Mg	Si	N	Ne	χ^2/dof
Since T_0	(keV)	$(10^{22} \text{ cm}^{-2})$		$(10^{22} \text{ cm}^{-2})$	$(s cm^{-3})$	$(s cm^{-3})$	$(s cm^{-3})$	$(s cm^{-3})$		- C				,
1.9	$6.4^{+0.3}_{-0.4}$	$5.4^{+0.4}_{-0.3}$	$0.87^{+0.03}_{-0.05}$	$3.5^{+0.3}_{-0.4}$	0.06 ± 0.05	0.04 ± 0.02	0.23 ± 0.04	$0.54^{+0.07}_{-0.06}$	1.09 ± 0.09	1.0	1.0	1.0	1.0	195.85/124
2.7	$8.3^{+0.4}_{-0.2}$	5.3 ± 0.4	$0.81^{+0.02}_{-0.03}$	2.5 ± 0.1	$0.09^{+0.01}_{-0.02}$	$0.034^{+0.009}_{-0.005}$	0.17 ± 0.03	0.50 ± 0.03	1.43 ± 0.08	1.0	1.0	1.0	1.0	418.60/134
3.5	$17.1^{+0.6}_{-2.5}$	$4.2^{+0.2}_{-0.1}$	0.88 ± 0.01	1.66 ± 0.09	0.03 ± 0.02	0.08 ± 0.01	0.35 ± 0.03	$0.44^{+0.02}_{-0.03}$	1.23 ± 0.07	1.0	1.0	1.0	1.0	624.98/136
4.6	24^{+1}_{-3}	2.5 ± 0.1	0.88 ± 0.2	1.12 ± 0.07	0.05 ± 0.02	0.059 ± 0.01	0.35 ± 0.02	0.45 ± 0.03	1.16 ± 0.07	1.0	1.0	1.0	1.0	736.36/144
5.5	6.9 ± 0.2	$8.8^{+0.7}_{-0.6}$	0.71 ± 0.1	1.36 ± 0.03	0.19 ± 0.03	0.04 ± 0.01	0.35 ± 0.03	$0.82^{+0.06}_{-0.04}$	0.78 ± 0.05	1.0	1.0	1.0	1.0	533.59/144
6.6	6.0 ± 0.2	$7.8^{+0.6}_{-0.5}$	0.74 ± 0.01	1.10 ± 0.04	0.12 ± 0.03	$0.041^{+0.007}_{-0.008}$	0.29 ± 0.03	$0.85^{+0.06}_{-0.07}$	0.72 ± 0.05	1.5 ± 0.2	1.6 ± 0.2	1.0	1.0	344.11/148
7.6	5.1 ± 0.2	$6.7^{+0.6}_{-0.5}$	0.70 ± 0.02	1.05 ± 0.04	0.06 ± 0.03	0.06 ± 0.01	$0.29^{+0.04}_{-0.03}$	$0.76^{+0.08}_{-0.07}$	0.63 ± 0.05	1.2 ± 0.1	1.2 ± 0.1	1.0	1.0	229.33/142
8.6	4.4 ± 0.2	5.7 ± 0.5	0.69 ± 0.02	0.99 ± 0.04	0.06 ± 0.03	0.06 ± 0.01	0.28 ± 0.03	$0.66^{+0.07}_{-0.06}$	0.61 ± 0.05	1.2 ± 0.1	1.1 ± 0.1	1.0	1.0	279.24/141
10.4	3.9 ± 0.1	$4.7^{+0.6}_{-0.4}$	$0.66^{+0.03}_{-0.02}$	0.98 ± 0.04	0.05 ± 0.03	0.07 ± 0.01	0.25 ± 0.03	$0.59^{+0.07}_{-0.06}$	0.59 ± 0.05	1.1 ± 0.1	0.9 ± 0.1	1.0	1.0	258.08/138
11.4	3.3 ± 0.2	3.7 ± 0.5	0.64 ± 0.04	0.99 ± 0.04	$0.03^{+0.04}_{-0.03}$	0.08 ± 0.01	0.22 ± 0.03	0.53 ± 0.07	$0.58^{+0.08}_{-0.07}$	1.1 ± 0.1	0.9 ± 0.1	1.0	1.0	247.30/123
12.3	2.9 ± 0.1	$3.4^{+0.5}_{-0.4}$	0.63 ± 0.04	1.02 ± 0.04	0.06 ± 0.04	0.08 ± 0.01	0.22 ± 0.03	0.45 ± 0.06	$0.59^{+0.09}_{-0.08}$	1.1 ± 0.1	0.8 ± 0.1	1.0	1.0	273.20/126
12.5	2.9 ± 0.1	$3.4^{+0.6}_{-0.5}$	0.62 ± 0.05	0.99 ± 0.05	$0.04^{+0.04}_{-0.03}$	0.08 ± 0.01	0.19 ± 0.03	0.47 ± 0.07	$0.57^{+0.1}_{-0.09}$	1.1 ± 0.2	0.9 ± 0.1	1.0	1.0	227.36/122
13.5	$2.77^{+0.07}_{-0.08}$	$2.7^{+0.4}_{-0.3}$	0.53 ± 0.04	$0.97^{+0.04}_{-0.03}$	$0.06^{+0.03}_{-0.02}$	$0.059^{+0.009}_{-0.007}$	0.16 ± 0.02	0.39 ± 0.04	$0.64^{+0.06}_{-0.05}$	1.1 ± 0.1	0.94 ± 0.09	1.0	1.0	603.94/145
15.2	2.5 ± 0.2	$2.7^{+1.7}_{-0.8}$	0.4 ± 0.1	1.08 ± 0.05	$0.05^{+0.07}_{-0.04}$	$0.09^{+0.02}_{-0.01}$	0.15 ± 0.03	0.30 ± 0.06	$0.5^{+0.2}_{-0.1}$	$0.9^{+0.2}_{-0.1}$	0.8 ± 0.1	1.0	1.0	243.71/108
16.1	2.27 ± 0.09	$2.2^{+0.7}_{-0.5}$	0.4 ± 0.1	1.04 ± 0.04	$0.08^{+0.05}_{-0.04}$	0.08 ± 0.01	0.13 ± 0.02	0.27 ± 0.04	$0.7^{+0.2}_{-0.1}$	$1.1^{+0.2}_{-0.1}$	$0.89^{+0.1}_{-0.08}$	1.0	1.0	378.70/125
17.2	1.86 ± 0.09	$2.1^{+0.4}_{-0.3}$	0.6 ± 0.1	1.02 ± 0.04	$0.17^{+0.07}_{-0.06}$	$0.11^{+0.02}_{-0.01}$	0.13 ± 0.02	0.25 ± 0.04	$1.0^{+0.3}_{-0.2}$	1.2 ± 0.2	0.90 ± 0.09	1.0	1.0	410.77/127
17.8	1.98 ± 0.09	1.7 ± 0.3	0.90 ± 0.04	0.99 ± 0.04	$0.14^{+0.05}_{-0.04}$	0.09 ± 0.01	0.12 ± 0.02	0.19 ± 0.03	$1.1^{+0.3}_{-0.2}$	$1.2^{+0.2}_{-0.1}$	0.95 ± 0.09	1.0	1.0	421.09/127
19.6	1.79 ± 0.06	1.8 ± 0.5	1.0	1.00 ± 0.04	$0.16^{+0.04}_{-0.03}$	0.09 ± 0.01	0.09 ± 0.01	0.18 ± 0.02	1.0	1.1 ± 0.1	0.9 ± 0.1	11^{+3}_{-2}	0.9 ± 0.1	453.54/127
21.5	$1.78^{+0.03}_{-0.02}$	0.79 ± 0.02	1.0	0.24	0.09 ± 0.02	0.069 ± 0.005	0.065 ± 0.007	0.12 ± 0.01	1.0	0.98 ± 0.08	0.92 ± 0.06	20^{+3}_{-1}	0.8 ± 0.1	581.42/142
22.6	1.67 ± 0.05	0.81 ± 0.03	1.0	0.24	0.12 ± 0.03	0.081 ± 0.008	0.07 ± 0.01	0.09 ± 0.02	1.0	0.89 ± 0.09	$0.84^{+0.04}_{-0.07}$	10^{+2}_{-1}	0.6 ± 0.1	474.39/127
23.7	1.59 ± 0.05	0.78 ± 0.03	1.0	0.24	0.10 ± 0.02	0.072 ± 0.006	$0.049^{+0.008}_{-0.007}$	0.11 ± 0.01	1.0	1.12 ± 0.09	0.99 ± 0.07	9 ± 1	1.0	456.94/136
24.5	1.60 ± 0.03	0.72 ± 0.02	1.0	0.24	0.07 ± 0.01	0.065 ± 0.005	$0.044^{+0.006}_{-0.005}$	0.11 ± 0.01	1.0	1.19 ± 0.07	1.0	10 ± 1	1.0	536.08/130
25.5	1.48 ± 0.03	0.71 ± 0.02	1.0	0.24	$0.08^{+0.02}_{-0.01}$	0.063 ± 0.005	$0.041^{+0.007}_{-0.005}$	$0.094^{+0.007}_{-0.01}$	1.0	$1.22^{+0.06}_{-0.05}$	1.0	20 ± 2	1.0	610.73/133
26.8	1.39 ± 0.04	0.74 ± 0.03	1.0	0.24	0.09 ± 0.02	0.067 ± 0.007	0.044 ± 0.007	0.07 ± 0.01	1.0	$1.17^{+0.08}_{-0.07}$	1.0	30 ± 4	1.0	594.59/132
27.6	$1.14^{+0.03}_{-0.02}$	0.77 ± 0.02	1.0	0.24	$0.18^{+0.02}_{-0.03}$	0.059 ± 0.005	0.07 ± 0.01	0.047 ± 0.006	1.0	$1.01^{+0.08}_{-0.06}$	1.0	37^{+4}_{-3}	1.0	703.18/140
28.5	1.29 ± 0.03	0.68 ± 0.02	1.0	0.24	0.09 ± 0.02	$0.061^{+0.005}_{-0.003}$	$0.029^{+0.006}_{-0.007}$	0.08 ± 0.01	1.0	$1.27^{+0.06}_{-0.07}$	1.0	15 ± 2	1.0	558.17/134
29.6	1.21 ± 0.03	0.68 ± 0.02	1.0	0.24	0.10 ± 0.02	$0.059^{+0.006}_{-0.005}$	$0.026^{+0.007}_{-0.009}$	0.07 ± 0.01	1.0	$1.30^{+0.09}_{-0.08}$	1.0	23 ± 3	1.0	605.34/133
30.6	0.83 ± 0.01	$0.68^{+0.03}_{-0.02}$	1.0	0.24	$0.15^{+0.04}_{-0.03}$	0.023 ± 0.005	0.03 ± 0.01	0.114 ± 0.004	1.0	$1.25^{+0.08}_{-0.09}$	1.0	105^{+10}_{-19}	1.0	568.5/134
31.6	0.99 ± 0.01	0.66 ± 0.02	1.0	0.24	$0.13^{+0.01}_{-0.02}$	0.040 ± 0.005	0.03 ± 0.01	$0.068^{+0.002}_{-0.004}$	1.0	$1.32^{+0.08}_{-0.06}$	1.0	63^{+10}_{-8}	1.0	619.63/127
32.6	1.24 ± 0.03			0.24	0.09 ± 0.02	$0.010^{+0.01}_{-0.009}$	0.03 ± 0.01	0.039 ± 0.009	1.0	1.0	1.0	1.0	1.0	116.64/104
33.6	1.19 ± 0.03			0.24	0.09 ± 0.02	0.02 ± 0.01	0.02 ± 0.01	0.05 ± 0.01	1.0	1.0	1.0	1.0	1.0	71.92/101
34.6	1.12 ± 0.03	•••	•••	0.24	0.11 ± 0.02	0.01 ± 0.01	0.02 ± 0.01	0.04 ± 0.01	1.0	1.0	1.0	1.0	1.0	81.14/90
37.7	1.03 ± 0.06	•••	•••	0.24	0.09 ± 0.03	$0.02^{+0.01}_{-0.02}$	$0.008^{+0.01}_{-0.008}$	0.04 ± 0.01	1.0	1.0	1.0	1.0	1.0	87.74/98
38.6	1.01 ± 0.04	•••	•••	0.24	$0.09^{+0.02}_{-0.01}$	0.02 ± 0.01	$0.009^{+0.01}_{-0.009}$	0.04 ± 0.01	1.0	1.0	1.0	1.0	1.0	103.56/96
39.7	0.96 ± 0.03	•••	•••	0.24	$0.09^{+0.03}_{-0.02}$	$0.03^{+0.01}_{-0.02}$	$0.004^{+0.01}_{-0.004}$	$0.041^{+0.009}_{-0.006}$	1.0	1.0	1.0	1.0	1.0	82.77/95

Note. The errors are 90% confidence limits. T_0 is defined as the start of the optical eruption at MJD 59434.5. Degrees of freedom are denoted "dof."

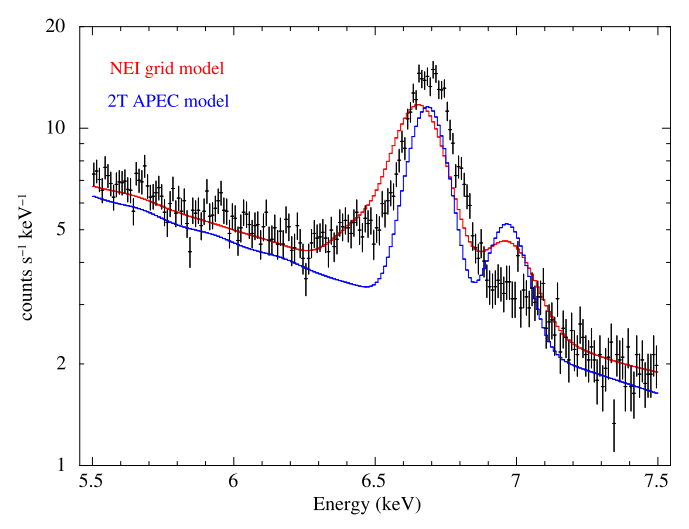


Figure 5. Fe-line region of a NICER spectrum taken around day 4. The plot, which covers 5.5–7.5 keV, shows He-like and H-like Fe lines. The red curve shows the fit to the Fe emission lines using the NEI grid model described in Section 3.2. The blue curve shows the fit to the Fe emission lines using a two-temperature velocity-broadened and thermally broadened collisional equilibrium plasma emission model, bvapec, convolved with a fully covering photoelectric absorption model, Tbabs. The NEI grid model describes the emission around 6.2–6.5 keV better than the two-temperature APEC model.

distribution of circum-binary material deviates significantly from the distribution expected by a spherically symmetric wind from the RG. The X-ray emission during the first several weeks of the RS Oph eruption (before day 40) most likely arose from plasma that was shock heated as the ejecta ran into circumstellar and circum-binary material. For any plasmas with kT above a few keV, cooling is dominated by Bremsstrahlung process and the cooling time is always \sim 1000 times longer than the time it takes plasma to reach ionization equilibrium. At a given point in time, X-ray-emitting plasma with a higher density-weighted ionization timescale is closer to ionization equilibrium—and likely more dense—than plasma with a lower density-weighted ionization timescale. So, the evolution of the four vnei component normalizations provides information about the density distribution through which the shocks propagated. For shocks moving into a spherically symmetric wind with a monotonically decreasing density profile, we might expect the N1 and N2 normalizations for emission from lower-density plasma to initially be low, with the N3 and N4 normalizations for emission from higher-density plasma initially high. After the shocks move into a lowerdensity plasma, N1 and N2 increase as N3 and N4 drop. We observed the expected behavior for N3 and N4, suggesting that some shocks did indeed move through material with high density near the binary and a strongly decreasing density profile. The importance of high ionization timescale components between day ~ 6 and ~ 17 (N3 and N4, respectively) suggests near-ionization-equilibrium plasma dominated the X-ray emission at this epoch. That N1 and N2 were fairly constant throughout the first 40 days of the eruption, however, hints at some shocks propagating through lower-density regions from the earliest days of the eruption. Such evolution of the N1, N2, N3, and N4 vnei normalizations is consistent with an RG wind distribution in RS Oph that is concentrated near the orbital plane, as suggested by Booth et al. (2016). Deviation from a spherical geometry was also suggested as a

possible interpretation of the rapid decline in X-ray flux by Sokoloski et al. (2006).

To explain the evolution of the emission components with different density-weighted ionization timescales, we envision a simple two-zone picture in which spherically symmetric nova ejecta collided with a dense equatorial ring (one of the two zones) and low-density material in roughly conical, polar regions (the other zone). In fact, the observations do indicate that the circum-binary region consists of dense equatorial structure and less dense, bipolar regions. In particular, for over 5 yr after the 2006 eruption, bipolar X-ray emitting flows appear to have maintained a tangential velocity of 4600 km s⁻¹, which requires the presence of virtually undecelerated ejecta in the polar directions (Montez et al. 2022). This suggests that, in the polar directions, the density is considerably lower than what a spherically symmetric toy model would suggest. Because X-ray emission is proportional to the square of the density, we expect the early X-ray emission to have been likely dominated by the shock driven into the equatorial ring. Therefore, even if the two zones subtended similar solid angles, the X-ray luminosities of these two zones are heavily weighted toward the denser region. When the ejecta interacted with the densest regions of the RG wind, near the orbital plane, higher density-weighted ionization timescales of 10^{11-12} s cm⁻³ were dominant, and hence the plasma producing most of the early emission reached equilibrium quickly. After day 18, when the shocks from ejecta interacting with wind in the less dense bipolar regions started to become more important, the contribution to the EM from the regions with higher densityweighted ionization timescales of 10^{11-12} s cm⁻³ decreased, and the contribution from regions with lower density-weighted ionization timescales of $10^{9-10}\,\mathrm{s\,cm}^{-3}$ started dominating (Figure 6(c)). The EM decreased as the ejecta expanded into the less dense environment (Figure 6(b)).

The basic two-zone picture supported by the X-ray monitoring of RS Oph may also explain a feature of the very-high-energy (VHE) emission from RS Oph in eruption. The GeV Fermi-LAT lightcurve peaked on day 2 after the start of the optical eruption, and the TeV HESS lightcurve peaked on day 5. Cheung et al. (2022) modeled this delay in the peak of the observed TeV emission compared to Fermi GeV emission as the consequence of different particle acceleration timescales in a single-zone shock by, whereas Diesing et al. (2023) modeled the delay with multiple shocks in the ejecta interacting with the asymmetric environment around the WD. Although our X-ray observations do not distinguish between these two models for the GeV and TeV emission, they do support the idea that distinct zones in the circum-binary environment gave rise to shocks with different properties.

4.2. Origin of the Observed Temperature and EM Evolution

Figure 1 shows that the NICER count rate in the broad, soft, and hard energy bands increased through day 6 and then remain at a similar count-rate level in the broad and soft energy bands up to day 21, whereas the count rate in the hard band monotonically decreased after day 6. An initial increase in the temperature through day 5, when $kT \sim 24 \text{ keV}$, is seen in Figure 6(a). It may be that a single shock dominates during these early times, whose energy goes into thermal X-rays and particle acceleration, with the efficiency of particle acceleration declining (Cheung et al. 2022), raising the X-ray temperature as it does so. Alternatively, there may be fast and slow shocks at

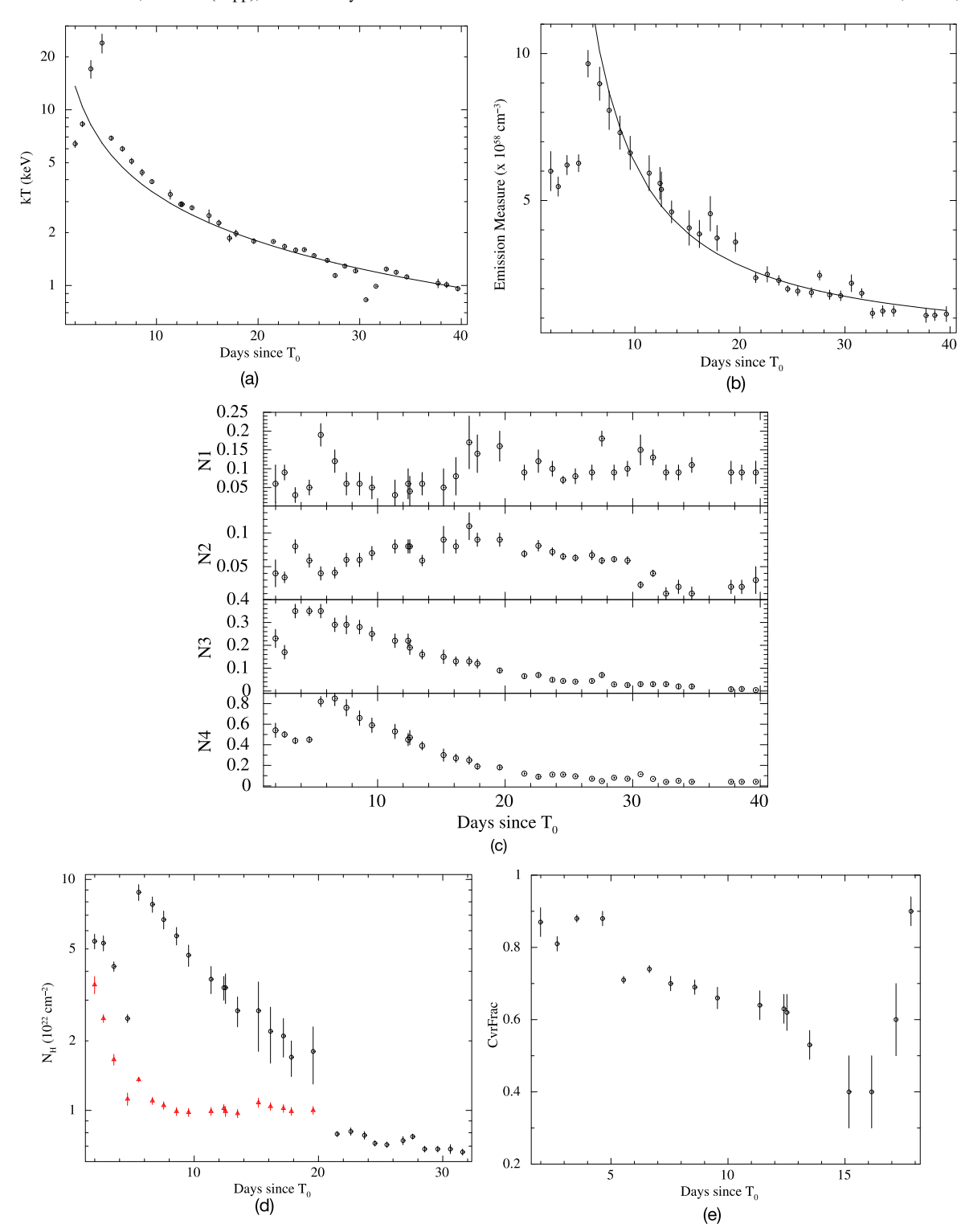


Figure 6. The evolution of various spectral parameters during the first few weeks of the eruption ($T_0 = \text{MJD}$ 59434.5), estimated by fitting the 1 day averaged NICER spectrum using the NEI grid model described in Section 3.2. (a) evolution of kT, fitted with a power law with an index of -0.9 ± 0.1 (solid line). (b) Evolution of the EM estimated by adding the normalizations of the four vnei components and described by a power law with an index of -1.2 ± 0.1 . (c) Normalizations of the different vnei components: N1 is the normalization of the component with a density-weighted equilibrium timescale of 10^9 s cm^{-3} , N2 is that with $10^{10} \text{ s cm}^{-3}$, N3 is that with $10^{11} \text{ s cm}^{-3}$, and N4 is that with $10^{12} \text{ s cm}^{-3}$. (d) Evolution of the variable absorption component from the RG wind and unshocked ejecta (N_{Hw} is represented by the black circles) and the absorption component due to the photoelectric absorption component along the line of sight (N_{H} is shown with the red triangles) in units of 10^{22} cm^{-2} . (e) Evolution of the partial covering fraction (CvrFrac). CvrFrac remained at 1.0 after day 18, indicating that the absorber fully covered the source from day 18 onwards.

these early times, as Diesing et al. (2023) argued to explain the GeV and TeV gamma-ray lightcurves, with the power in the slow shock peaking early and then the power in the fast shock

peaking around day 5. The continued cooling when the nonequilibrium component became dominant requires an explanation other than radiative cooling. Deceleration of the

ejecta is unlikely in the low-density, polar directions, while it is quite plausible in the equatorial region. An explanation for the evolution of the emission behind the polar shocks is explored in the next paragraph.

So far, we have focused the possibility of NEI effects. Another effect is possible for even younger and/or lowerdensity shocks: the electron temperature may be considerably lower than the ion temperature (see, e.g., Masai 1984; Raymond et al. 2023). Moreover, it is the electron temperature that we derive through X-ray spectral fitting, which, in such a case, cannot be used to derive the shock velocity. The initial postshock temperature of electrons, in the absence of Coulomb collisions or other heating processes, would be of order m_e/m_p lower than the shock temperature, so the emission of X-rays in RS Oph proves that the electrons are heated. In the context of supernova remnants, $T_e/T_i \sim 0.1$ appears consistent with observations (Matsuda et al. 2022), and interpreted as due to collisionless electron heating. We speculate that, at late times during the NICER monitoring campaign, the timescale for postshock Coulomb heating became longer and longer as the ejecta density further decreased. In such a situation, it is plausible for us to observe lower T_e as X-ray emission is dominated by material in the earlier phases of the gradual Coulomb heating. Montez et al. (2022) observed a constant temperature ($kT \sim 0.2 \text{ keV}$), freely expanding X-ray emission region about \sim 5 yr after the 2006 eruption. This may indicate a $kT_{\rm shock} \sim 20 \,\rm keV$ (expected for a strong shock given the inferred expansion velocity of the order of 4500 km s⁻¹) in which $T_e/T_i \sim 0.01$. At earlier times, the observed electron temperature might represent an electron population which is gradually heated up toward the shock temperature, with timescales that depends on the local density.

The EM plot in Figure 6(b) shows a sudden increase in the value around day 6. A likely scenario explaining the sudden jump in the EM could be of the ejecta interacting with a dense clump of matter around the equatorial ring, which is predicted by the hydrodynamical simulations of Booth et al. (2016). Luna et al. (2020) reported a brightening in RS Oph in 2017 in the *V* band using AAVSO lightcurves, presumably implying that the accretion rate through the disk increased. We speculate that this may have been caused by an episode of enhanced mass loss from the RG and that this same enhancement could have produced an unaccreted clump of matter outside the binary that slowly (with a velocity of the order of $10 \,\mathrm{km \, s^{-1}}$) expanded. This previously ejected clump will be at a reasonable distance from the binary for the 2021 nova ejecta to plow into this region approximately 5 days after the start of the eruption.

The actual circum-binary density structure around RS Oph is certainly even more complex than our two-zone scenario. Any density diagnostics from observed X-ray emission may apply to the densest regions, and may or may not provide constraints on the density of the polar cones. Sokoloski et al. (2006) interpreted the evolution of the X-ray spectrum of RS Oph during the 2006 eruption as due to a decelerating shock (they also considered departure from spherical symmetry). While this finding is consistent with a two-zone picture of a dense equatorial torus and near-empty polar regions, it is likely to be an oversimplification. The situation more likely involves a continuous gradient of density going from equatorial to polar directions. The simulations by Booth et al. (2016) further suggest that clumps in the circum-binary regions are likely. In any case, it is highly probable for systems like

RS Oph to have some dense regions (with shocked plasma in ionization equilibrium) and some low-density regions where shocked plasma remains out of ionization equilibrium in the early stages of the nova.

Additional asymmetries due to the finite distance between the WD and RG are likely to have a negligible effect on the observed X-ray emission. A spherically symmetric wind from the RG with a mass loss rate of $10^{-7}~M_{\odot}~\rm yr^{-1}$ and a velocity of $10~\rm km~s^{-1}$ would have a density of $2.2\times10^9~\rm cm^{-3}$ at a distance (from the center of the RG) of 1 au. Its density goes as r^{-2} , where r is the distance from the center of the RG. Ejecta with a velocity of $5000~\rm km~s^{-1}$ would travel 3 au day $^{-1}$, compared to the binary separation of ~ 1 au. Therefore, after several days, the fact that the nova ejecta originate from the WD, not the RG, leads to only a small perturbation of a simple, spherically symmetric picture. The wind density encountered by the ejecta on day 5 would be about $9\times10^7~\rm cm^{-3}$ in this example. Such a wind is sufficiently dense to reach ionization equilibrium (which requires $nt\sim10^{12}~\rm s~cm^{-3}$; Smith & Hughes 2010) on a timescale much smaller than the age of the nova eruption.

4.3. Variable, Partial Covering Absorption

In the early days of the eruption, the preexisting wind nebula —including the equatorial density enhancement (Ribeiro et al. 2009; Booth et al. 2016)—provided a significant source of absorption. This absorbing material had density structures on the scale of the X-ray-emitting region, as suggested by the spectral fits with a covering fraction less than one. Another potential source of intrinsic absorption is the unshocked portion of the ejecta or a portion of the ejecta was shocked but underwent catastrophic cooling (Derdzinski et al. 2017). Throughout the eruption, the X-ray emission emanated from the shocked shell surrounding unshocked ejecta interior to it. In such a situation, X-rays from the near side of the shell are unabsorbed by the interior matter, while those from the far side are absorbed. The evolution of the column density and covering fraction of the absorber constrain the density structure of the circum-binary material and unshocked ejecta. From Figure 6(d), the column density of the absorption decreased with time after its peak of almost 10^{23} cm⁻² on day 6. This is consistent with the early time X-ray emitting shock moving through the dense circum-binary ring. The density of the equatorial enhancement remaining in front of the shock decreases with time as the shock propagates into the lowerdensity regions. In addition, the covering fraction of the absorber declined from 1.0 (absorber fully covering the source) at the start of the eruption to 0.4 on day 16 (Figure 6(e)), indicating strong changes in the circum-binary absorbing material and/or the X-ray emission region itself. In the early days of the eruption, the RG wind outside the nova ejecta contributed the bulk of the intrinsic absorption. After the first few NICER observations, the X-ray-emitting region had a significant size compared to that of the binary; our lines of sight to different parts of the X-ray emitting plasma passed through different amounts of RG wind. By around day 16, the nova ejecta had expanded to such a degree that the wind nebula outside the ejecta likely provided little absorption. Instead, it may have been the unshocked nova ejecta (surrounded by the shocked shell) that provided the intrinsic absorption. The front side of the shocked shell was seen only through interstellar absorption, while the back side could have also been absorbed by the unshocked ejecta, resulting in a partial covering fraction close to, but less than 0.4, as we observed around day 16. The rise in covering fraction back to one by around day 18 is consistent with the drop in absorbing column at around that same time to the interstellar value.

5. Summary

- 1. The 2021 eruption of the recurrent nova RS Oph was monitored extensively by NICER. Neither single- nor two-temperature collisionally ionized plasma (APEC) model with variable abundances and velocity-broadened and thermally broadened emission lines could adequately model the line emission from the K shells of medium-Z elements such as Ne, Mg, and Si. The APEC models also led to large residuals below approximately 1 keV. We therefore used an alternative approach to modeling the NICER spectra by using a grid of NEI collisional plasma components with a single temperature and four density-weighted ionization timescales, along with a partial covering absorber.
- 2. The evolution of the normalizations of the spectral components with different density-weighted ionization timescales can be understood if the X-ray emission during approximately the first two weeks of the eruption was dominated by shocks propagating through circum-binary material concentrated in the equatorial plane. Because the timescale required for shocked gas to achieve ionization equilibrium is inversely proportional to the square of the gas density, dense shocked regions reach ionization equilibrium more quickly than less dense regions, where the shocked gas remains out of equilibrium for longer. During the first two weeks, emission from plasma close to ionization equilibrium, where the high density-weighted ionization timescales of 10^{11} – $10^{12}\,\mathrm{s\,cm^{-3}}$, was dominant. After day 18, the interaction between the ejecta and the less dense circum-binary material in the polar regions became more evident, the contribution to the EM from plasma with the higher density-weighted ionization timescales of 10^{11} – 10^{12} s cm⁻³ decreased, and the contribution from plasma out of ionization equilibrium, with lower density-weighted ionization timescales of $10^9 - 10^{10}$ s cm⁻³ became important. After day 6, the EM monotonically decreased as a power law with index -1.2 ± 0.1 .
- 3. After peaking at around 10²³ cm⁻², the column density absorbing the X-rays followed a decline. This behavior is consistent with the X-ray emission initially being dominated by shocks related to the ejecta interacting with the dense circum-binary ring around the binary and then shocks associated with expansion into the lower-density polar regions. The partial covering absorption fraction decreased from near unity at the start of the eruption to 0.4 on day 16, as expected if absorption around day 16 was primarily due to unshocked ejecta.
- 4. Although some ambiguity is introduced into the interpretation of the temperature evolution by our use of a single temperature to describe X-ray emission from behind multiple shocks, we move forward with such an interpretation assuming that one shock dominated the X-ray emission at any given time. The evolution of the temperature of the nonequilibrium plasma, *kT*, shows an initial increase through day 5, with a peak value of 24 keV (Figure 6(a)). The peak in the temperature around days 4–7 is roughly coincident with the enhancement in

- X-ray intensity in the MAXI 10–20 keV GSC lightcurve (Figure 2). The initial rise in the X-ray temperature could have been associated with a decrease in the shock power going into particle acceleration, which can lead to rapid cooling of the postshock plasma. The detection of RS Oph in GeV and TeV gamma rays shows that particle acceleration was present in the early days of the 2021 eruption. After day 5, the temperature decreased as a power law with an index of -0.9 ± 0.1 as the eruption evolves, close to the expected decline rate for a shock heated by a decelerating blast wave moving into a stellar wind (Sokoloski et al. 2006).
- 5. The sudden increase in the EM around day 6 was possibly due to interaction between the nova ejecta and a clump of matter previously ejected from the RG. We speculate that an episode of enhanced mass loss from the RG about 5 yr prior to the nova could have produced such a clump while simultaneously explaining the optical brightening observed in the AAVSO lightcurves during 2017.

Acknowledgments

We thank the anonymous referee for constructive comments which helped improve the manuscript. We thank Marina Orio and Juan Luna for helpful discussions. The scientific results reported here are based on observations made by the NICER X-ray observatory and we thank the NICER team for scheduling and executing these Target of Opportunity observations. This research has made use of MAXI data provided by RIKEN, JAXA, and the MAXI team. This research has made use of data and/or software provided by the High Energy Astrophysics Science Archive Research Center (HEASARC), which is a service of the Astrophysics Science Division at NASA/GSFC. J. L.S. acknowledges support from NASA grant 80NSSC21K0715 and NSF award AST-1816100. N.I. acknowledges support from NASA grant 80NSSC21K1994.

ORCID iDs

Nazma Islam https://orcid.org/0000-0002-2413-9301

References

```
Acciari, V. A., Ansoldi, S., Antonelli, L. A., et al. 2022, NatAs, 6, 689
Badenes, C., Borkowski, K. J., Hughes, J. P., Hwang, U., & Bravo, E. 2006,
    ApJ, 645, 1373
Bailer-Jones, C. A. L., Rybizki, J., Fouesneau, M., Demleitner, M., &
   Andrae, R. 2021, AJ, 161, 147
Bamba, A., Yamazaki, R., Yoshida, T., Terasawa, T., & Koyama, K. 2005,
   ApJ, 621, 793
Bode, M. F., & Evans, A. 2008, Classical Novae (2nd ed.; Cambridge:
  Cambridge Univ. Press)
Bode, M. F., O'Brien, T. J., Osborne, J. P., et al. 2006, ApJ, 652, 629
Booth, R. A., Mohamed, S., & Podsiadlowski, P. 2016, MNRAS, 457, 822
Borkowski, K. J., Lyerly, W. J., & Reynolds, S. P. 2001, ApJ, 548, 820
Brandi, E., Quiroga, C., Mikołajewska, J., Ferrer, O. E., & García, L. G. 2009,
    A&A, 497, 815
Cheung, C. C., Ciprini, S., & Johnson, T. J. 2021, ATel, 14834, 1
Cheung, C. C., Johnson, T. J., Jean, P., et al. 2022, ApJ, 935, 44
Derdzinski, A. M., Metzger, B. D., & Lazzati, D. 2017, MNRAS, 469, 1314
Diesing, R., Metzger, B. D., Aydi, E., et al. 2023, ApJ, 947, 70
Eitner, P., Bergemann, M., Ruiter, A. J., et al. 2023, A&A, 677, A151
Enoto, T., Maehara, H., Orio, M., et al. 2021, ATel, 14850, 1
Ferrigno, C., Savchenko, V., Bozzo, E., et al. 2021, ATel, 14855, 1
```

Gendreau, K. C., Arzoumanian, Z., Adkins, P. W., et al. 2016, Proc. SPIE,

9905, 99051H

```
H. E. S. S. Collaboration, Aharonian, F., & Ait Benkhali, F. 2022, Sci, 376, 77
Hjellming, R. M., van Gorkom, J. H., Taylor, A. R., et al. 1986, ApJL,
   305, L71
Kaastra, J. S., & Bleeker, J. A. M. 2016, A&A, 587, A151
Luna, G. J. M., Carrera, R., Enoto, T., et al. 2021, ATel, 14873, 1
Luna, G. J. M., Sokoloski, J., Mukai, K., & Kuin, P. 2020, ATel, 13810, 1
Masai, K. 1984, Ap&SS, 98, 367
Matsuda, M., Uchida, H., Tanaka, T., Yamaguchi, H., & Tsuru, T. G. 2022,
   ApJ, 940, 105
Matsuoka, M., Kawasaki, K., Ueno, S., et al. 2009, PASJ, 61, 999
Mikolajewska, J., Aydi, E., Buckley, D., Galan, C., & Orio, M. 2021, ATel,
Montez, R., Luna, G. J. M., Mukai, K., Sokoloski, J. L., & Kastner, J. H. 2022,
   ApJ, 926, 100
Munari, U., & Valisa, P. 2021, arXiv:2109.01101
Nelson, T., Donato, D., Mukai, K., Sokoloski, J., & Chomiuk, L. 2012, ApJ,
Ness, J. U., Beardmore, A. P., Bode, M. F., et al. 2023, A&A, 670, A131
O'Brien, T. J., Bode, M. F., Porcas, R. W., et al. 2006, Natur, 442, 279
Okajima, T., Soong, Y., Balsamo, E. R., et al. 2016, Proc. SPIE, 9905, 99050Z
Orio, M., Behar, E., Drake, J., et al. 2021, ATel, 14906, 1
Orio, M., Behar, E., Luna, G. J. M., et al. 2022, ApJ, 938, 34
Orio, M., Gendreau, K., Giese, M., et al. 2023, ApJ, 955, 37
Orlando, S., Drake, J. J., & Laming, J. M. 2009, A&A, 493, 1049
Page, K. L. 2021, ATel, 14894, 1
```

```
Page, K. L., Osborne, J. P., & Aydi, E. 2021, ATel, 14848, 1
Peters, W. M., Clarke, T. E., Giacintucci, S., Kassim, N. E., & Polisensky, E.
  2021, ATel, 14908, 1
Raymond, J. C., Ghavamian, P., Bohdan, A., et al. 2023, ApJ, 949, 50
Ribeiro, V. A. R. M., Bode, M. F., Darnley, M. J., et al. 2009, ApJ, 703, 1955
Rout, S. K., Srivastava, M. K., Banerjee, D. P. K., et al. 2021, ATel, 14882, 1
Rupen, M. P., Mioduszewski, A. J., & Sokoloski, J. L. 2008, ApJ, 688, 559
Shidatsu, M., Negoro, H., Mihara, T., et al. 2021, ATel, 14846, 1
Smith, R. K., & Hughes, J. P. 2010, ApJ, 718, 583
Smith, R. K., Valencic, L. A., & Corrales, L. 2016, ApJ, 818, 143
Sokoloski, J. L., Luna, G. J. M., Mukai, K., & Kenyon, S. J. 2006, Natur,
  442, 276
Sokoloski, J. L., Rupen, M. P., & Mioduszewski, A. J. 2008, ApJL, 685, L137
Sokolovsky, K., Aydi, E., Chomiuk, L., et al. 2021, ATel, 14886, 1
Sokolovsky, K. V., Mukai, K., Chomiuk, L., et al. 2020, MNRAS, 497, 2569
Starrfield, S., Iliadis, C., & Hix, W. R. 2016, PASP, 128, 051001
Sugizaki, M., Mihara, T., Serino, M., et al. 2011, PASJ, 63, S635
Vink, J. 2012, A&ARv, 20, 49
Wagner, S. J. 2021, ATel, 14844, 1
Warner, B. 1995, Cataclysmic Variable Stars, Vol. 28 (Cambridge: Cambridge
  Univ. Press)
Williams, D., O'Brien, T., Woudt, P., et al. 2021, ATel, 14849, 1
Woodward, C. E., Banerjee, D. P. K., Evans, A., et al. 2021a, ATel, 14910, 1
Woodward, C. E., Evans, A., Banerjee, D. P. K., et al. 2021b, ATel, 14866, 1
```

Page, K. L., Beardmore, A. P., Osborne, J. P., et al. 2022, MNRAS, 514, 1557